



# City Research Online

## City, University of London Institutional Repository

---

**Citation:** Kovacevic, A. (2017). Algebraic generation of single domain computational grid for twin screw machines. Part II. Validation. *Advances in Engineering Software*, 109, pp. 31-43. doi: 10.1016/j.advengsoft.2017.03.001

This is the accepted version of the paper.

This version of the publication may differ from the final published version.

---

**Permanent repository link:** <https://openaccess.city.ac.uk/id/eprint/17006/>

**Link to published version:** <https://doi.org/10.1016/j.advengsoft.2017.03.001>

**Copyright:** City Research Online aims to make research outputs of City, University of London available to a wider audience. Copyright and Moral Rights remain with the author(s) and/or copyright holders. URLs from City Research Online may be freely distributed and linked to.

**Reuse:** Copies of full items can be used for personal research or study, educational, or not-for-profit purposes without prior permission or charge. Provided that the authors, title and full bibliographic details are credited, a hyperlink and/or URL is given for the original metadata page and the content is not changed in any way.

---

---



**Algebraic Generation of Single Domain Computational Grid for Twin Screw Machines**  
**Part II – Validation**

Ahmed Kovacevic, Sham Rane\*

Centre for Compressor Technology, City, University of London, EC1V 0HB, London, U.K.

Email: [sham.rane@city.ac.uk](mailto:sham.rane@city.ac.uk), Tel: +44(0) 20 70408795,

\* Corresponding Author

**Abstract**

Algebraic procedures are available to generate computational grid for CFD analysis of twin screw compressors. Recently new algebraic method was formulated to generate numerical grids for CFD calculation of twin screw machines with grids generated from outer casing boundaries [16, 18]. In this paper, the grids of Rotor to Casing and Casing to Rotor type are tested for performance calculation of a dry air screw compressor using ANSYS CFX solver and the results have been compared with measurements. Firstly the base-line grid of the Rotor to Casing grid type was used to obtain CFD results. A grid independent solution was obtained for this base-line grid. The size of the mesh thus obtained has been used with other grid variants for comparison. A set of successively refined Casing to Rotor grid type was tested by increasing the density of nodes on the rotor profile in the interlobe leakage region. A gradual improvement in the accuracy of flow prediction was achieved with successive refinement in the interlobe region. The third variant used for comparison is a Casing to Rotor grid type with a single rotor domain that has no interface between the rotor blocks. A significant improvement in the prediction of flow and internal pressure was achieved. These developments have also extended the capability of the deforming grids to be used with other CFD solvers like STAR-CCM+ and ANSYS FLUENT. Due to fully hexahedral cell structure and improved global grid quality, addition of physical phenomena like oil injection in the models has now become achievable.

## Keywords

Computational Fluid Dynamics, Algebraic Grid Generation, Twin Screw Compressors, Deforming Grid, Positive Displacement Compressors.

## Nomenclature

$\phi_w$	- wrap angle [Degree]	$\rho_0$	- suction density [ $\text{kg}/\text{m}^3$ ]
$z_1$	- number of lobes on main rotor [-]	$rpm, n$	- rotor speed [rpm]
$z_2$	- number of lobes on gate rotor [-]	$\dot{m}$	- mass flow rate [ $\text{kg}/\text{min}$ ]
$\alpha$	- male rotor rotation angle [Degree]	$P_i$	- indicated power [W]
$\eta_v$	- volumetric efficiency [%]	$\dot{V}$	- volumetric flow rate [ $\text{m}^3/\text{min}$ ]
$P_{si}$	- specific indicated power [ $\text{kW}/\text{m}^3/\text{min}$ ]	$\eta_m$	- mechanical efficiency [%]
$T_m$	- Main rotor torque [N m]	$T_g$	- Gate rotor torque [N m]

## Abbreviations

RC – Distribution from Rotor boundary to the Casing boundary	CR – Distribution from Casing boundary to the Rotor boundary
--	--

## 1 Introduction

The work presented in Part I of this paper was the implementation of a procedure for generation of twin screw rotor grids with the boundary distribution governed from the non-rotating outer casing to the rotating inner rotors (CR type grids). CR grid type distribution gave the advantage of a non-rotating outer boundary. Two control functions were introduced to get fast regularisation of the initial algebraic distribution. One was an analytical sine function and the other was a background blocking procedure for guiding the initial algebraic distribution on the rotor boundary. In this Part II of the paper, the CR type grids have been tested for performance calculation of a dry air screw compressor.

The application of RC type algebraic grids was previously reported in several studies [1, 2, 3, 4]. The early references can be found in the thesis by *Kovačević*, [2] and the manuscript *Kovačević et al.* [4]. In these works, the analysis of three vital case studies was reported that form the first instance of any full 3D transient computational activity on twin screw compressors. The solution was obtained using COMET solver. One of the case studies was with a dry air screw compressor in which two different rotor profiles were compared using CFD results for their performance. The second case study was of an oil injected screw compressor where oil was treated as a passive scalar. The distribution of oil in the compression chamber and the comparison of results with measurements were presented. This case also forms the first validation of the RC type of grids. Flow delivery and indicated power was found in a good agreement with the measurements. The deviation was about 10% and 8% respectively. The third

analysis was of an oil injected ammonia refrigeration screw compressor with the real gas definition of the equation of state.

More recently, *Pascu et al.* [8] have reported optimisation of the discharge port of a Twin screw compressor using the RC type of algebraic grids and ANSYS CFX solver. Optimisation was based on the selection of the port geometry by relative comparison of flow fields predicted by the CFD models. *Sauls and Branch* [11] used the same grid type to obtain results from CFD calculations with Ansys CFX to develop an improved one-dimensional thermodynamic model for refrigeration screw compressors, by extracting calibration coefficients that influence the pressure variation during the discharge process. *Kovačević and Rane* [5] reported an analysis of a dry air twin screw expander using this type of the mesh. This report was the first validation of the RC type grids in expander applications. Flow and indicated power as well as internal pressure variation curve were compared with the measurements carried out at TU Dortmund. These analysis highlighted that prediction of indicated power from CFD models was in good agreement over the range of filling pressure and rotor speeds. But at high filling pressures and low rotor speeds there was a large deviation in the predicted gas flow through the expander. This large variation was attributed to changes in clearances during the operation [12]. In another recent study by *Kovačević et al.* [6], the RC type of grids were used to solve flow in dry air compressor using two different flow solvers. One solver was a coupled vertex-centre based solver ANSYS CFX and the other solver was segregated cell-centre based formulation from Simerics Pumplinx. Both were pressure based solvers. The performance indicators of pressure variation in the compressor chamber, mass flow rate, indicated power and the volumetric efficiency were used for comparison. Analysis showed a big influence of the solver and mesh treatment on the flow predictions of the two solvers. *Rane et al.* [9, 10] extended the RC type grid generation to variable geometry rotors such as variable lead and variable profiles and reported cases on comparison of the performance of these different rotor geometries.

On the application of CR type of grid structure, *Vande Voorde, Vierendeels and Dick* [13, 14] were the first to implement a grid generation algorithm for block structured mesh from the solution of the Laplace equation for twin screw compressors and pumps using differential methods and then construct a CR type of rotor grid to be used for final calculations. In his thesis, *Vande Voorde* [13, 14] presented the solution of flow in a double tooth compressor and an oil free twin screw compressor. The results were compared with experimental data over a range of discharge pressures and rotor speeds. A larger deviation in the volumetric efficiency and specific work was reported at lower rotor speeds. More recently, *Papes, Degroote and Vierendeels* [7] presented a 3D CFD analysis of an oil injected twin screw expander using the same differential CR type grid generation approach. A real gas model for the working fluid R245fa was used and results for the different leakage flows were presented together with chamber pressure variation curves and performance analysis at different pressure ratios.

The test case presented here uses the CR type grid structure with algebraic implementation and background blocking regularisation approach described in Part I of this paper [18]. The study has two objectives.

- First is to verify that the new CR type algebraic grid structure implemented in Part I [18] produces cells that are valid and within quality requirements of the flow solver.
- The second objective is to compare the model results under similar set of operating conditions with measured performance and understand the influence of interlobe grid refinement and non-conformal rotor to rotor interface on the accuracy of performance predictions.

It is expected that the new CR type grids will allow for better accuracy in predictions from the flow solver because of the fully hexahedral cell structure. It is also expected that the elimination of the non-conformal interface will improve robustness of the solver.

## 2 Measurements on the test screw compressor

Figure 1a shows the 3D CAD model of the test compressor and Figure 1b shows its rotors. The rotors are designed with ‘N’ profile with 3 lobes on the main rotor and 5 lobes on the gate rotor. The rotor centre distance is 93.00 mm and the main rotor length to outer diameter ratio is 1.6. The compressor has an axial suction and a combined axial and radial discharge. The built in volume index is set to be 1.8 and the wrap angle on the main rotor is 285 degree. The design clearances of the machine are 120 to 160 micro meters in all, the rotor interlobe gaps, radial rotor to casing clearance gaps and the high pressure end clearance gap.

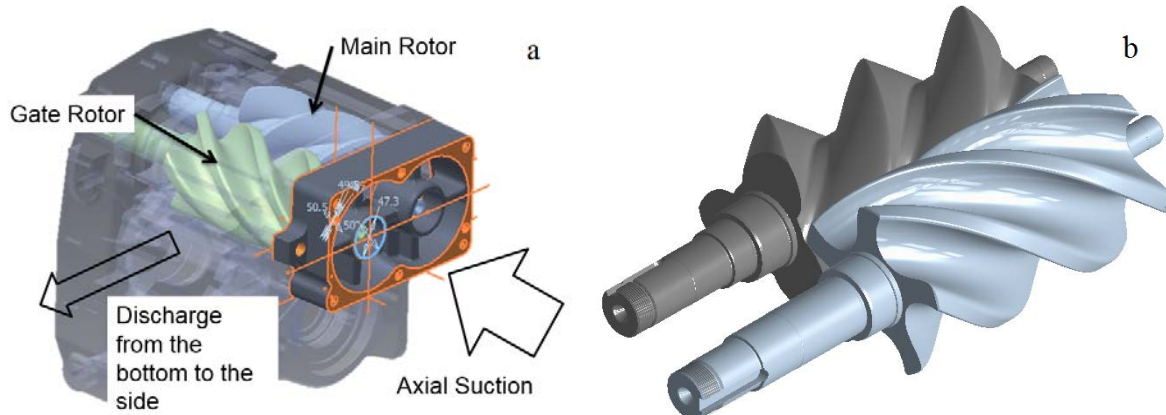


Figure 1 Test screw compressor at City University London – a) The machine, b) Rotor pair

This oil free compressor is used for dry air compression in the range of operating speeds from 6000 to 12000 rpm. The suction is at atmospheric conditions and the maximum discharge pressure for safe temperature limits is about 3.0 bar. The compressor runs under synchronised operation and both the rotors are driven by timed two stage helical gear box integral with the compressor housing.

Test measurements of the compressor performance were carried out in the air compressor test rig at City University London. Figure 2 shows the layout of the measurement rig its main components and measurement points. The compressor is driven by a variable speed 75kW motor and has an internal synchronising gear box with the gear ratio 7.197:1. The speed of the motor is adjusted using a variable frequency drive. The torque meter is installed on the motor shaft while the digital encoder for the speed measurement is mounted on the male rotor shaft.

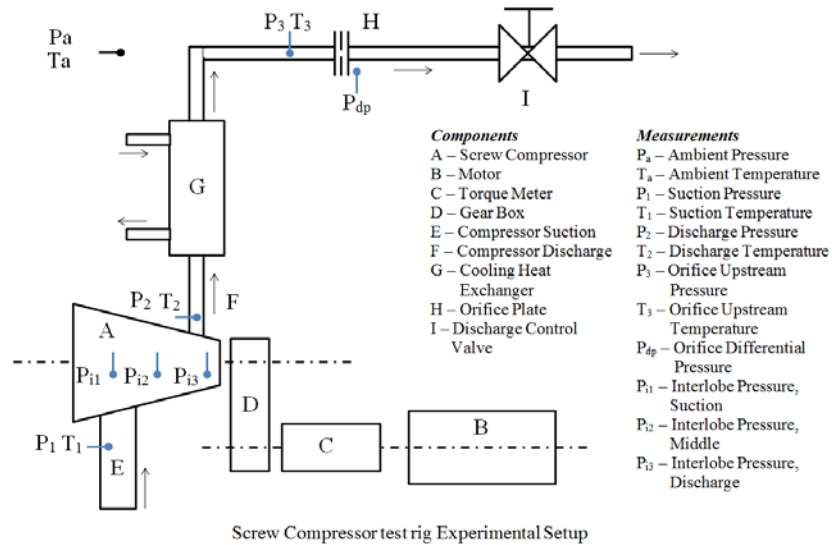


Figure 2 Experimental setup for performance measurement

The discharge pressure is controlled via a check valve (I) in the discharge line. Gas flow rate is measured using an orifice meter (H) in the discharge line. Since the discharge gas temperature is high in the absence of oil cooling, a cross flow water heat exchanger (G) is installed to cool the gas before it enters the main discharge line in the rig. Figure 3a shows the compressor in the test rig. Speed encoder on the main rotor shaft, suction and discharge pressure transducer and discharge temperature thermocouple are visible.

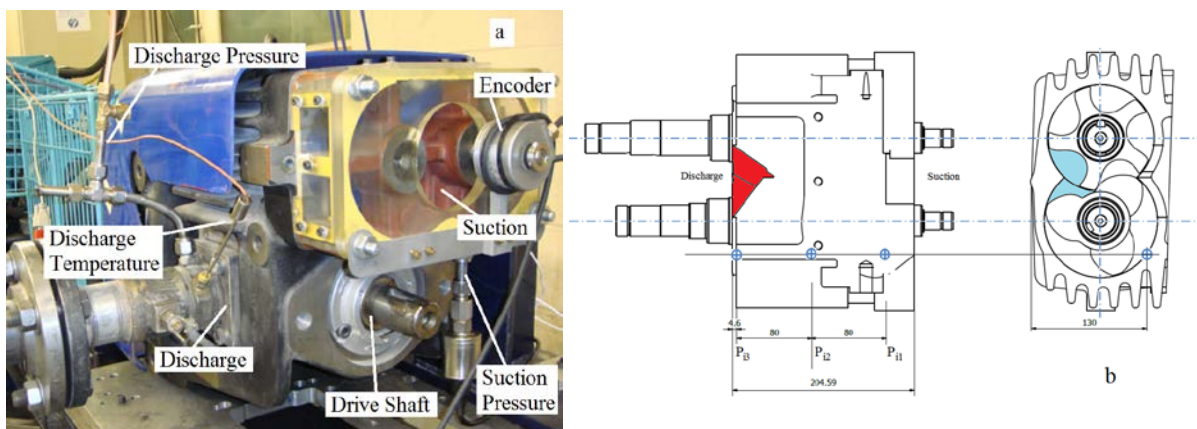


Figure 3 Test compressor – a) Rig, b) Location of interlobe pressure transducers

The pressure and temperature of the gas are measured at the inlet, discharge and upstream of the orifice plate. In addition, three pressure transducers are used for recording the interlobe pressures and are located in the working chamber through the compressor casing on the male rotor side. Figure 3b shows the location of the dynamic interlobe pressure transducers in the compressor housing. Measurement data acquisition is carried out using CompactRIO (CRI0-9022) system from National Instruments and Labview software. The measurements were taken for discharge pressures up to 2.5bar and speeds from 6000 to 8000rpm. Table 1 presents the instrumentation and transducer details used in the test rig. BS ISO 1217:2009 has been followed in setting the rig and measurement uncertainties have been estimated for mechanical power and flow rate measurements (*Bianchi and Cipolloni, [15, 17]*) to be used for comparison of CFD results.

Table 1 Test rig instrumentation and transducer details.

Measured Parameter	Transducer	Specifications
Compressor Speed, N	Shaft Encoder (BHG 16.25W.3600-B2-5)	360 TTL pulses per revolution Accuracy= $\pm 10\%$
Compressor Torque, T	TRP-500Torque meter ( strain gauge transducer)	Max capacity: 500Nm, Calibration level: 335Nm Range = 0 - 6000 rpm, Supply volt=10v dc, Accuracy= 0.25 % of max capacity
Inlet pressure, P <sub>1</sub>	PDCR 110/w -Pressure Transducer	Operating range = 3.5bar(abs) Excite voltage=10V dc, Accuracy =0.6%,
Outlet pressure, P <sub>2</sub>	PDCR 922-Pressure transducer	Operating range =15 bar (abs) Excite voltage=10V dc, Output voltage= 100 mV Accuracy =0.6%
Orifice plate differential pressure, P <sub>dp</sub>	PDCR 2120- Pressure transducer	Pressure diff= 0.35 bar, Excitation Voltage=10V dc, Accuracy= 0.6%,
Orifice plate inlet press, P <sub>3</sub>	PDCR 922-Pressure transducer	Operating range =15 bar (abs) Excite voltage=10V dc, Output voltage= 100 mV Accuracy =0.6%
Interlobe Pressure, P <sub>i1</sub> , P <sub>i2</sub> , P <sub>i3</sub>	XTME 190 M Series – Pressure transducer Inorganically Bonded Piezoresistive Sensor	Operating range =35 bar g Excite voltage=10V dc, Output voltage= 75 mV Sensitivity =2.14 mV/bar g Range= -55 <sup>0</sup> C to 235 <sup>0</sup> C
Inlet temperature , T <sub>1</sub> Outlet temperature, T <sub>2</sub> Orifice plate inlet Temperature, T <sub>3</sub>	Platinum Resistance Thermometer	Range= -75 <sup>0</sup> C to 350 <sup>0</sup> C, Accuracy= $\pm 0.5^0\text{C}$
Water Temp at the inlet and outlet of the cooler	K- type thermocouple ( based on Ni/Cr-Ni/Al alloy )	Range= -200 <sup>0</sup> C to 1300 <sup>0</sup> C, Accuracy= $\pm 2.2^0\text{C}$ sensitivity = 41 $\mu\text{V}/^{\circ}\text{C}$

Uncertainty in mechanical power measurement is introduced by shaft speed and torque transducers. Direct measurement uncertainty for speed is 10% and for torque it is 1.25Nm. Hence power measurement uncertainty is 10.9 – 11.1% from 8000 to 6000 rpm. In case of flow, the uncertainty is introduced mainly by the orifice upstream pressure transducer and thermocouple and the differential pressure transducer. The pressure transducers have direct measurement uncertainty of 0.6% each and for the thermocouple it is 0.5%. Hence uncertainty in flow measurement is 0.98% over the full range. Here accuracy is taken as the measurement uncertainty. Uncertainty in volumetric efficiency is same as flow and that in specific power is 11.04%.

### 3 Aspects of the CFD model

The compression chamber of the machine is divided into three main zones namely, the deforming rotor domain that is represented by a hexahedral grid structure. The rotor grid accounts for the radial tip leakage gaps, the rotor to rotor interlobe leakage gap and the blow-hole areas. The axial end leakage gap on the high pressure side is not included in this grid and if desirable can be added as a static mesh. Both the suction and discharge port geometries control the built in volume index of the compressor. The fluid volumes of these zones are extracted from the CAD models and generally tetrahedral grid structure with wall prism layers is preferred in these domains to capture the geometry. Figure 4 shows the three domains and boundaries of the CFD model. Also the suction and discharge port zones have been presented with their boundaries and interfaces with the rotor domain. At both the suction and discharge boundaries, the ports have been extended to provide uniform pressure conditions.

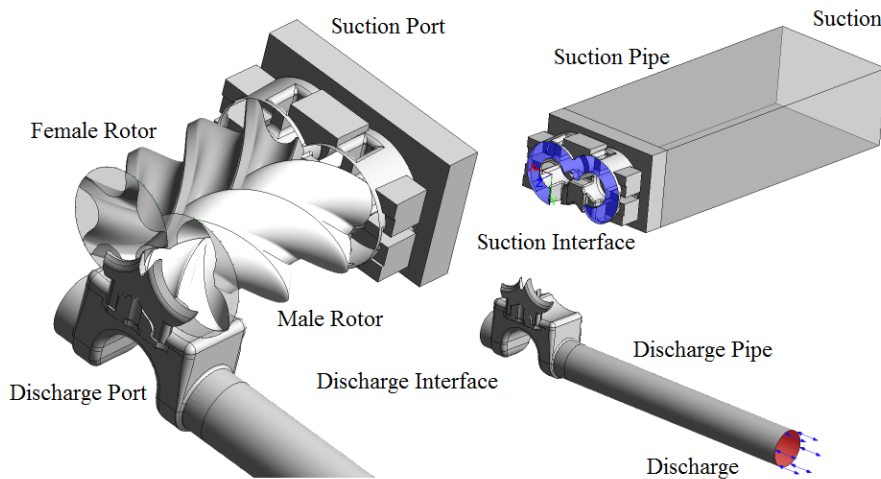


Figure 4 CFD Model Domain and Grid refinements in the interlobe clearance

During operation, the rotors are subjected to thermal deformation which changes the clearance gap size. It is estimated that the clearances will reduce with the increase in operating temperature. Therefore the grids for the CFD model are generated with reduced uniform clearances of 60 micro meters in the interlobe and radial gaps in order to compensate for thermal distortion. The CFD models used in the study do not take clearance changes into consideration and also the axial end clearances are not included in order to simplify the model. A uniform pressure of 1.0 bar was specified at the suction while the discharge pressure is 2.0bar. The main rotor speeds were 6000rpm and 8000rpm.

Table 2 CFD Solver parameters

Criteria	Selection	Remark	
<b>Turbulence model</b>	SST – k Omega	Flow regime is Turbulent	
<b>Inlet boundary condition</b>	Opening	Specified total pressure and temperature	Allows for flow to go in and out of the domain

<b>Outlet boundary condition</b>	Opening	Static pressure For backflow; total pressure and temperature	without creating wall faces
<b>Advection scheme</b>	Upwind	High resolution	Blends 1 <sup>st</sup> and 2 <sup>nd</sup> order
<b>Turbulence scheme</b>	First order upwind		
<b>Transient scheme</b>	Second order	Backward Euler	Fully implicit
<b>Inner coefficients</b>	Up to 20 iterations per time step		
<b>Convergence criteria</b>	5e <sup>-4</sup>	r.m.s residual level	
<b>Relaxation parameters</b>	Solver relaxation fluids	0.1 or lower	For stability

ANSYS CFX solver was used for calculation. The solver formulation is based on a vertex centred computational cell structure and pressure based coupled solution algorithm. The high resolution advection scheme was used in the solver and the main settings are listed in Table 2. Air was defined as an ideal gas with dynamic viscosity  $1.831 \times 10^{-5} \text{ kg m}^{-1} \text{ s}^{-1}$ , specific heat capacity  $1004.4 \text{ J kg}^{-1} \text{ K}^{-1}$  and thermal conductivity  $2.61 \times 10^{-2} \text{ W m}^{-1} \text{ K}^{-1}$ . The flow solution was converged well to get cyclic repetition of the flow and pressure pulsations across the boundaries. A cyclic average mass balance between the suction and the discharge was achieved within 1% in all cases.

### 3.1 Rotor boundary definition

In case of the base grid with RC type of structure, the two rotor blocks rotate with time in the flow solver. Because of this nature of deformation, the Cartesian components of mesh motion associated with nodes representing the rotor surface resolves the rotational speed of the rotors. This is shown in Figure 5a where no additional rotating wall definition is required for the rotors and the tangential velocity gets resolved by the mesh velocity.

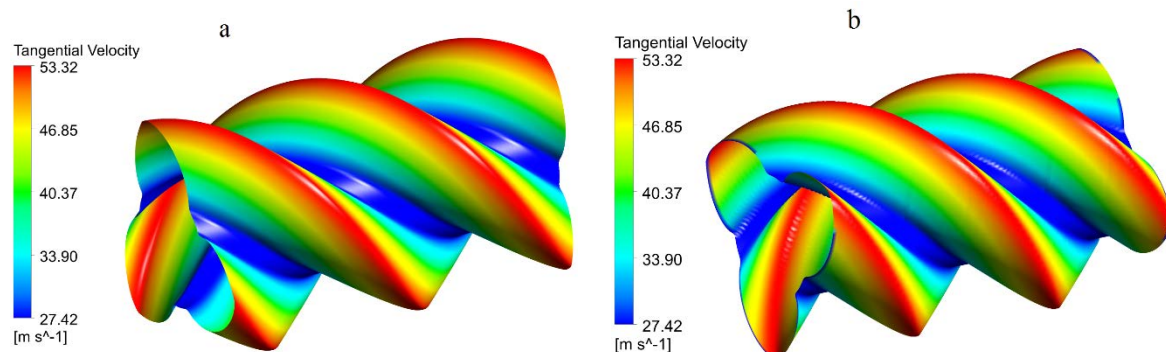


Figure 5 Specification of rotor boundary condition – a) RC type grid, b) CR type grid

In case of the new CR type of grid structure, the two rotor blocks are stationary in the global coordinate frame. With time the nodes slide on the rotor surface and interior nodes move to accommodate the deformation but these do not rotate. As such an external specification of boundary velocity is required for the nodes representing the rotor surface. The main rotor is rotating about the global z axis and is defined as a rotating wall with specified speed. A new coordinate system with its z-axis parallel to the global z axis is defined at the centre of the gate rotor. The gate rotor is defined as a rotating wall with specified speed about its local z axis. The tangential velocity is displayed in Figure 5b and it matches with that obtained from the rpm and rotor radii at all the nodes.

### 3.2 Grid dependence evaluation on the RC type grid

The results from the CFD modelling of a screw compressor are used in this study to compare the RC and CR grid types in the rotor flow domain. Therefore, it is essential to achieve the solution which is independent of increasing grid resolution. This is a very challenging task in screw compressor analysis due to the highly deforming grid. One factor of the grid that has direct influence on the performance is the resolution of the rotor profile grid. Hence a set of grids of the RC type were studied with increasing the node density on the rotor profile as listed in Table 3. In all cases the number of axial grid divisions and the size of the time step are maintained constant.

Table 3 RC grid type refinement

Name	Radial	Angular	Circumferential	Main	Gate	Total	Total
				Rotor	Rotor	Rotors	Mesh
<b>RC-1</b>	8	40	200	173727	173727	347454	648190
<b>RC-2</b>	8	50	250	268821	268821	537642	838378
<b>RC-3</b>	10	50	350	455532	458150	913682	1214418
<b>RC-4</b>	10	50	450	589050	589050	1178100	1478836
<b>RC-5</b>	10	50	600	785400	785400	1570800	1871536

Figure 6 shows the effect of grid refinement on the predicted integral quantities from the base grid such as the mass flow rate, indicated power and specific power. The discharge pressure was 2.0 bar and the main rotor speed was 8000rpm in these calculations. The mass flow rate (Figure 6a) showed an increase with the grid refinement. The difference between the consecutive grids is around 10% between RC-1 and RC-2 level but with further refinements of level RC-4 and RC-5 the change in mass flow rate reduced to less than 3%. This indicates that the rotor geometry is captured better with refined grids and results in the reduction of leakage losses. Similarly, the indicated power (Figure 6b) increases by 2-5% when the grid is refined between RC-1 and RC-2 levels but with further grid refinements the change in indicated power dropped to less than 0.8%. Figure 6c shows the influence on specific power. With refinements of level RC-4 and RC-5 the change in specific indicated power reduced to less than 2.5%

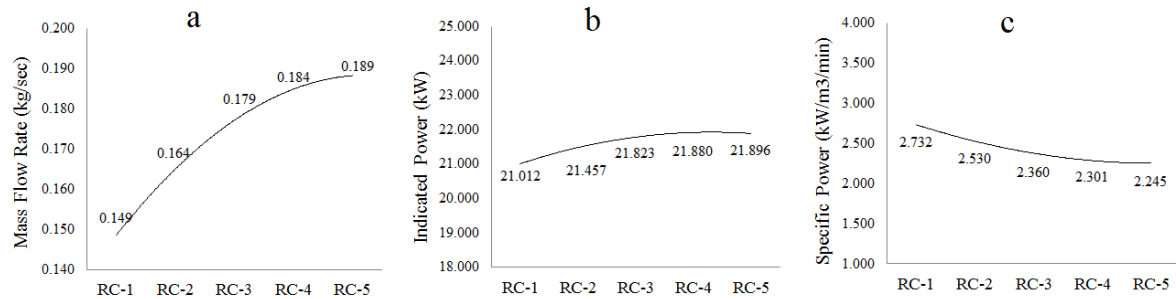


Figure 6 Effect of the grid refinement on integral parameters a) Mass Flow Rate, b) Indicated Power, c) Specific Power

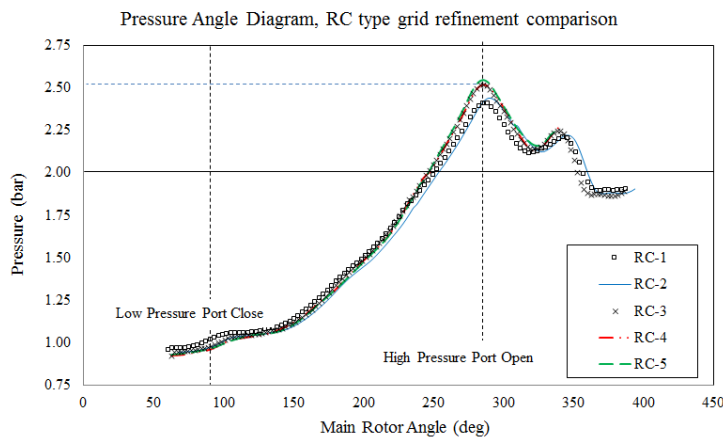


Figure 7 Effect of the RC grid refinement on the internal pressure in the compression chamber

The chamber pressure increased with grid refinement as shown in Figure 7. The grids RC-1 to RC-3, showed a very small influence on the change in pressure history during the compression process as well as in the peak pressure at the end of compression. This indicates that the increase in profile grid resolution has higher impact on the mass flow rate and leakage flow prediction than on the prediction of pressure history or indicated power. Relatively small influence on pressure variation is recorded even for further grid refinements from RC-3 to RC-5. Based on the analysis shown in Figure 6 and Figure 7, the RC-3 grid size has acceptable grid independence values of less than 3% change in flow and less than 0.8% in pressure and power. At the same time the computational resources demanded with levels RC-4 and RC-5 were increased exponentially compared to RC-3.

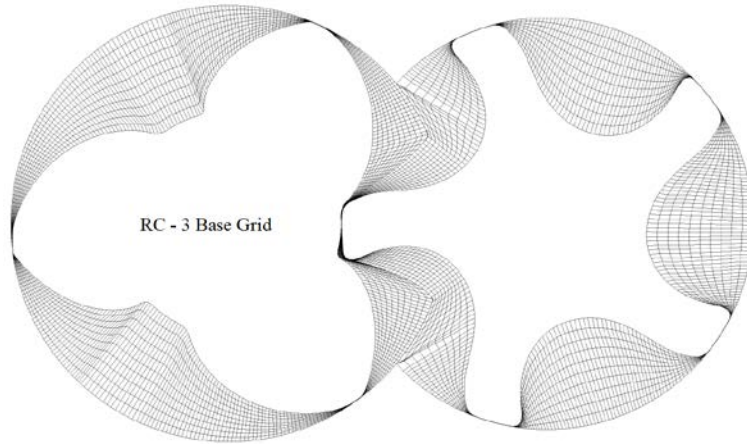


Figure 8 RC type grid structure – Based Grid, RC – 3 level grid refinement

Therefore the configuration of RC-3 grid was selected as the baseline grid size for further performance comparison of newly produced CR type grids. The cross section of the RC-3 grid is shown in Figure 8.

#### 4 Generation of CR type grids

Using the regularisation control method of the background blocking described in Part I [18], a set of CR type grids were generated for evaluation of performance predictions. The overall number of profile nodes was maintained the same in CR Grid-1 as in the RC-3 baseline grid. CR Grid-2 to CR Grid-4 feature successive refinement in the interlobe region as shown in Table 4. It was necessary to increase the number of circumferential nodes along the profile in order to achieve similar density of nodes in the casing part of the rotor when the number of interlobe nodes gradually increased. This is required for the fair comparison with the RC grid type. Figure 9a shows the cross section of the CR Grid-1 and Figure 9b shows the finest CR Grid-4 which has in total 600 nodes placed on the rotor in each cross section out of which 350 are in the interlobe space and remaining 250 on the outer circle.

Table 4 CR type grid level specification and number of divisions

Grid Type	Level	Radial	Angular	Circumferential			Rotor Mesh Size
				Total	Interlobe	Casing	
RC-3	Base Grid	10	50	350	n/a, ~90	260	913682
CR-1	Grid – 1	10	50	360	120	240	942480
CR-2	Grid – 2	10	50	400	150	250	1049818
CR-3	Grid – 3	10	50	450	200	250	1178100
CR-4	Grid – 4	10	50	600	350	250	1570800
CR Single	Grid – 5	6	50	350	80	270	581434

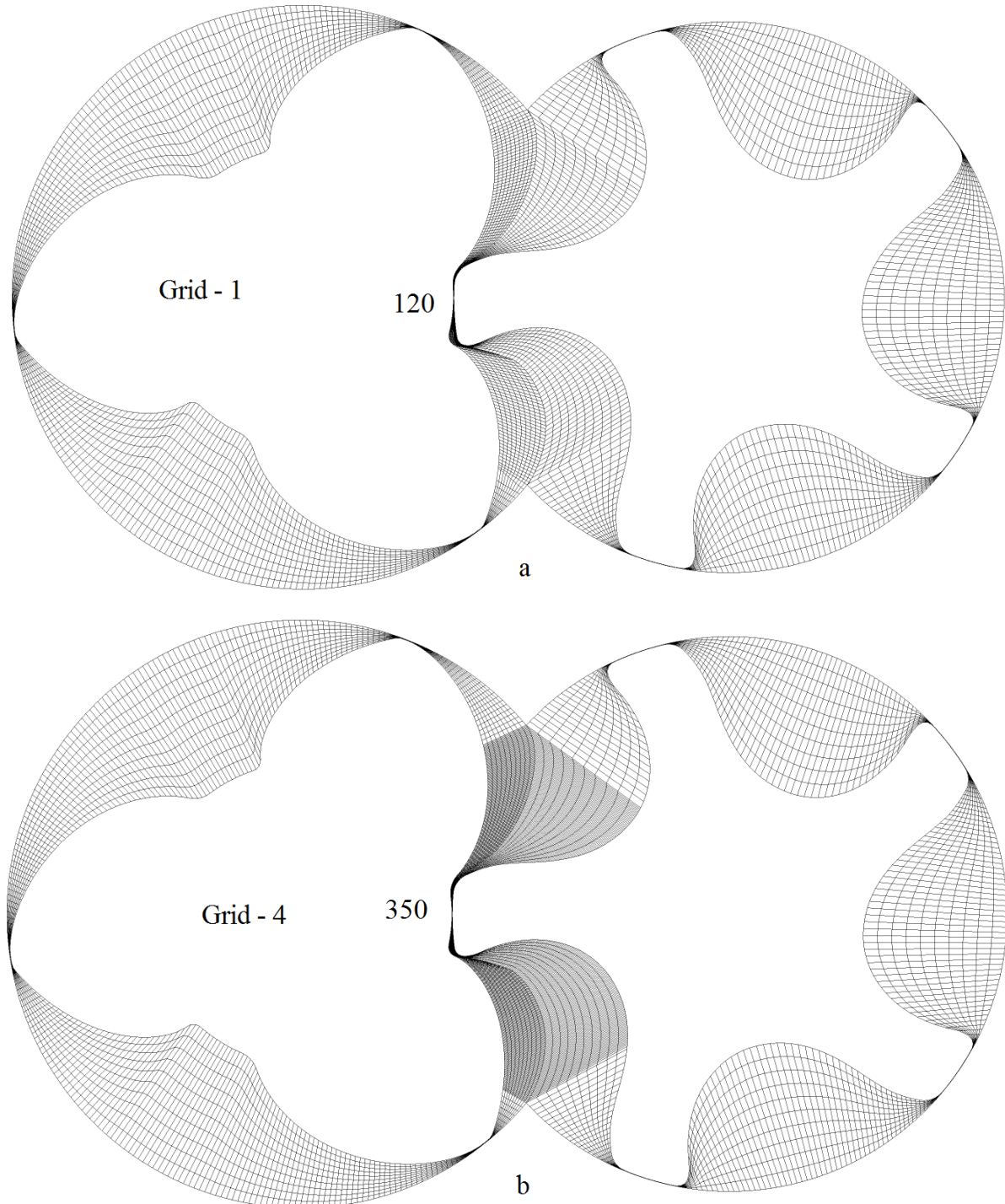


Figure 9 CR type grids showing refinements in the interlobe region a) Grid – 1, b) Grid – 4

The last grid shown in Table 4 is CR Grid–5. It is of the same size as CR Grid-1 but with the conformal node-to-node map between the rotor sub-domains. The rotor distribution was generated by use of the background blocking method described in Part I [18]. The CR Grid-5 is passed to the flow solver as a single structure without an interface between the two rotor subdomains which was achieved by merging nodes on the original conformal interface. Figure 10 shows the CR Grid-5 with single flow domain for both rotors in 2D cross section and the full 3D rotor mesh

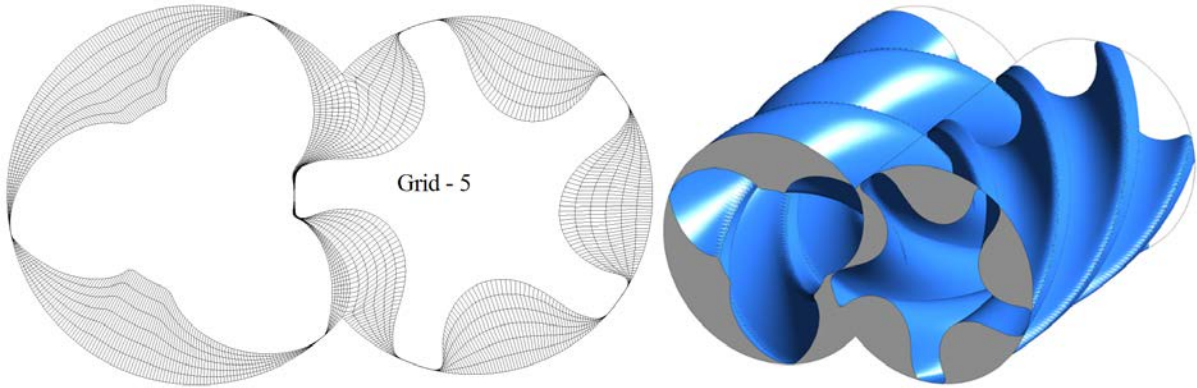


Figure 10 CR type Grid – 5 with single domain structure

All calculations have been performed using Ansys-CFX solver with identical settings and boundary conditions for all calculated cases. During calculations it was observed that the convergence of the solver with CR Grid–5 was more robust than others and compared to Grid -4 better relaxation factors of the coupled solver are specified for that grid while still the convergence of equations was faster (lower number of iterations per time step) as reported in Table 5. It should be noted that the calculation time are varying mainly because of the difference in total node density of the mesh between these grids.

Table 5 Solver performance at 8000rpm rotor speed for the grid variants

Grid Type	Level	Calculation time per time step (min)	Iterations required to converge per time step	Solution time for 300 time steps (hour)*	Error in cycle averaged mass flow (%)	Solver relaxation
RC-3	Base Grid	6.54	5 to 8	41.6	0.922	0.1
CR-1	Grid – 1	7.81	5 to 8	50.8	0.374	0.1
CR-4	Grid – 4	13.75	7 to 9	80.6	1.183	0.08
CR Single	Grid – 5	4.94	5 to 7	29.9	0.633	0.1

\* Includes reading and writing of files

## 5 Results and Discussion

In positive displacement machines, the internal pressure and temperature change due to change in the volume of the compression chamber. Due to the increased pressure the compressed gas tends to escape through the leakage gaps into chambers with lower pressures. Due to the nature of the compression process in positive displacement machines it is very difficult to visualise leakage flows by any experimental method. The accurate prediction of 3D flow within the working domain may help in visualizing and measuring that phenomenon in great details. The results obtained by CFD solution in the form of pressure distribution, temperature distribution and velocity of the gas in the compression chamber are used in this paper for comparison of various grids. The internal pressure changes obtained

by simulation are compared with the pressure changes measured in the working chamber. In addition, calculated integral performance parameters such as indicated power  $P_i$ , flow rate  $Q_i$ , volumetric efficiency  $\eta_v$  and specific indicated power  $P_{si}$  are compared with the test measurements.

### 5.1 Pressure distribution

Plots of the pressure distribution on the rotor surface at 8000rpm and 2.0 bar discharge pressure are shown in Figure 11. Figure 11a shows the RC-3 baseline grid on which grid independent results were achieved. Figure 11b shows the CR Grid-4 with the refined interlobe region and Figure 11c shows the CR Grid-5 with single domain mesh. Despite the surface representation of the rotor with RC type grid is much more regular than that obtained with CR grids, the pressure contours show similar variations in both grid structures.

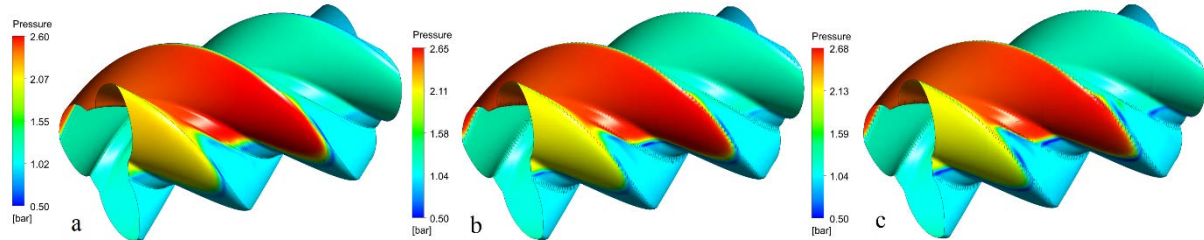


Figure 11 Pressure contours on the rotor surface – a) RC grid, b) CR Grid – 4, c) CR Grid – 5

The built in volume index is the ratio between suction and discharge chamber volume which in principle defines the size of the discharge port in screw compressors. For the built in volume index of 1.8 and the discharge pressure of 2.0 bar, the compressor is experiencing over-compression, i.e. the maximum pressure raises above the discharge pressure. Therefore the highest pressure in the machine occurs before the discharge port is open as shown in Figure 11. In comparison to the base grid CR-3, CR Grid-4 and CR Grid-5 both show a higher internal pressure of 0.5 and 0.8 bar respectively at this rotor position. This could be due to the better representation of the leakage paths along the sealing line which is in Figure 11 shown by large gradients of the pressure. It should be noted that pressure drop in the sealing strip is higher for CR grids than for RC grids which confirms the above statement.

### 5.2 Pressure – Angle variation

Figure 12a and Figure 12b show variation of pressure in the compression chamber at 6000 rpm and at 8000 rpm respectively. The discharge pressure was 2.0 bara. The over-compression is clearly visible in these diagrams. The calculated values closely follow the measured values represented by the black dotted line. Measured pressure uncertainty band is  $\pm 1\%$  full scale (0.35 bar) for Kulite's XTME 190 M series 35bara range transducers. Over-compression pressure is higher at 8000rpm than at 6000rpm. CFD predictions and measurements show similar pressure pulsations once the compression chamber opens to the discharge port.

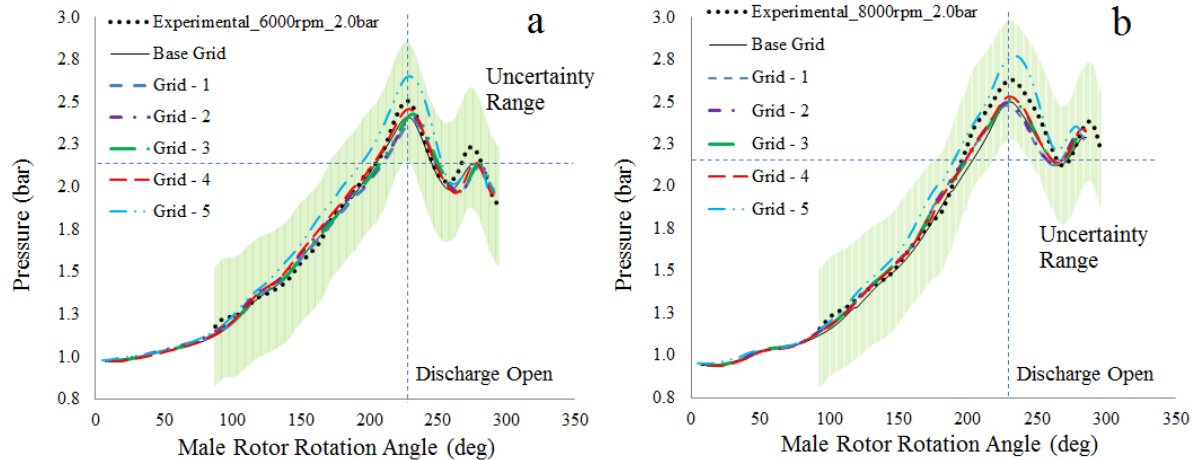


Figure 12 Pressure variation in the compression chamber with 2.0 bar – a) 6000rpm, b) 8000rpm

The internal pressure history predicted by the RC baseline grid and CR Grid-1 to Grid-4 show little difference between each other. A small increase in the compression rate is observed with Grid – 4 at both speeds. However, the peak pressure predicted by the CR Grid-5 with single domain is higher than others at both speeds. It is also noticeable that the pressure rises faster during the compression process with CR Grid-5 than with other grids or measurements. This indicates that CR Gird-5 with the single domain grid for both rotors, produces lower leakage through the leakage gaps during the compression process than grids with two sub-domains connected through a non-conformal interface despite the same geometry and setup. This relates to two issues:

- Since CR Grid-5 is with the single domain for both rotors, it has no sliding or stretching interface in the mesh. All other grids have that interface. This indicates that the method which the existing CFD solver uses to calculate fluxes over non-conformal interfaces is not fully conservative and it creates numerical dissipation across the interface and therefore higher leakage losses. Therefore, use of CR single domain grid is recommended for accurate calculation of leakage flows.
- Since the single domain grid offers more conservative solution, the clearances need to be adjusted to reflect the real situation better. The nominal clearances in the real compressor are 120  $\mu\text{m}$  while the clearances used in calculations were 60  $\mu\text{m}$ .

The difference between CFD predictions on both RC and CR meshes with two subdomains connected through a non-conformal interface and experimental peak pressures is higher at 8000rpm than at 6000rpm which could be due to the thermal deformation of rotors and casing. However, for the single domain mesh the predicted peak pressure is higher than measured and has a similar offset at both speeds. Therefore, firstly, it is necessary to adjust the clearances to capture accurately the leakage path size with CR single domain mesh and consequently asses methods to capture thermal distortions of the machine at different operating conditions which is recommended for future work.

### 5.3 Temperature distribution

The compressed gas which leaks from the compression chamber into parts of the compressor with lower pressure is trapped in these chambers where it had leaked to and is recompressed. Due to the recompression, its temperature increases further. This is detrimental to the performance of the machine.

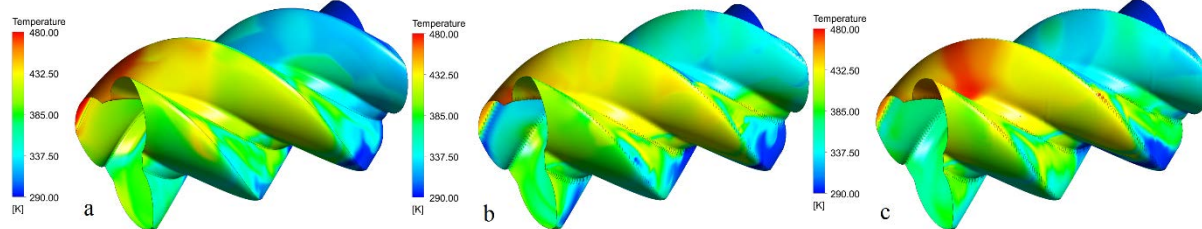


Figure 13 Temperature distribution on the rotor surface – a) RC grid, b) CR Grid – 4, c) CR Grid – 5

Figure 13 shows the temperature distribution of the gas on the rotor surface. Figure 13a is the baseline RC grid, Figure 13b is CR Grid – 4 with highest interlobe refinement and Figure 13c is single domain CR Grid – 5. The peak temperatures are similar in all calculated cases but a small difference in 3D distribution and non-homogeneity within each compression chamber is observed. Because of over-compression, the gas will have the highest temperature in the compression chamber just before it is opened to the discharge port. It is also noticeable that the gas temperature on the rotor surface is not as uniformly distributed as in the case of the chamber pressure.

### 5.4 Velocity distribution

By observing velocity levels in the rotor domain it is possible to identify zones of the higher leakage. The highest velocities are recorded across the interlobe gap where the domain with the peak pressure is directly connected through the clearance gaps to the domain with the low suction pressure. Similarly two consecutive compression chambers with different pressures are connected through the radial tip gaps where increased velocities are observed. Increased gas velocities and higher leakages are also expected in the blow-hole area on the high pressure side.

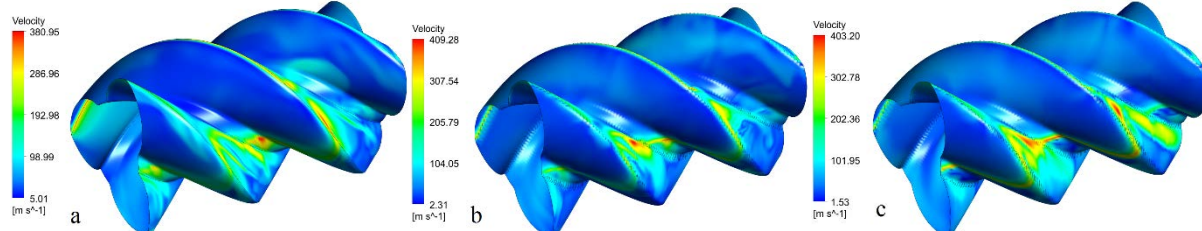


Figure 14 Velocity contours on the rotor surface – a) RC grid, b) CR Grid – 4, c) CR Grid – 5

Figure 14 show the contour plots of the magnitude of gas velocity adjacent to the rotor surface. The local zones of high velocity are in the leakage gaps. The peaks are profound in the interlobe leakages. The maximum velocity in the RC type base grid (Figure 14a) at this particular rotor position is nearly 380 m/s. The new CR type grids show a higher maximum velocity with 409 m/s in case of Grid – 4

(Figure 14b) and 403 m/s in the case of Grid – 5 (Figure 14c). These differences in velocity magnitude can be attributed to the higher peak pressures that were observed with the new CR grids which are in turn the consequence of better representation of leakage paths.

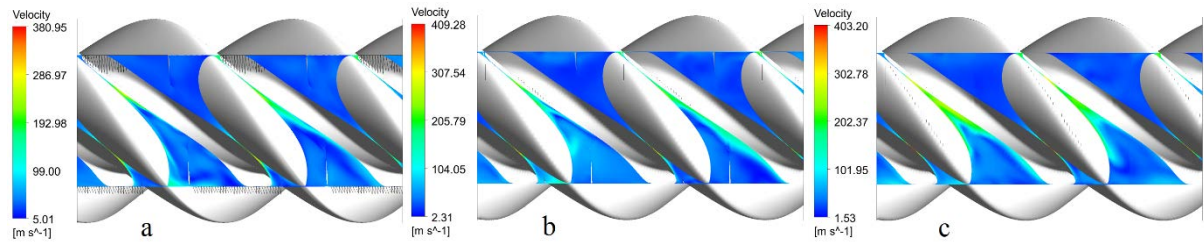


Figure 15 Velocity contours in the blow-hole section – a) RC grid, b) CR Grid – 4, c) CR Grid – 5

Figure 15 (a – RC Grid, b – CR Grid 4 and c – CR Grid 5) shows the variation of gas velocity in a section of the compression chamber passing through the blow-hole area. The velocity of gas through the blow-hole area is high but the magnitude is lower than that in the interlobe gaps. Also between the different grid types, same level of gas velocity is being recorded here. This indicates that the flow solver is able to use the warped faces at the small tip radii that were generated because of the new CR grid structure as effectively as the RC grid structure.

### 5.5 Indicated Power - $P_i$

The torque on each rotor is calculated from the CFD results from the surface pressure and the orientation and position of the rotor cell surface, Figure 11. The indicated power can then be calculated using equation 1 as,

$$P_i = \frac{2\pi n \left( T_m + \frac{z_1}{z_2} T_g \right)}{60} \quad (1)$$

The power of the test compressor is measured by the torque meter located on the driving shaft. This torque includes losses in the synchronising gear box and bearings. Based on the previous measurements of this compressor in the existing test rig and its measured indicator diagrams, it has been estimated that the compressor mechanical efficiency ( $\eta_m$ ) is 96% at 6000 rpm and it drops 1.4% for every 1000 rpm increase in speed. The estimated mechanical efficiency is used for calculation of the compressor mechanical losses which are then subtracted from the measured results to obtain the measured indicated power. For easier interpretation the predicted values of  $P_i$  are normalised to the corresponding measured values obtained on the test compressor in order to calculate the error in predicting indicated power. Figure 16 shows the difference in predicting indicated power for various calculated cases and the measured indicated power as a function of speed.

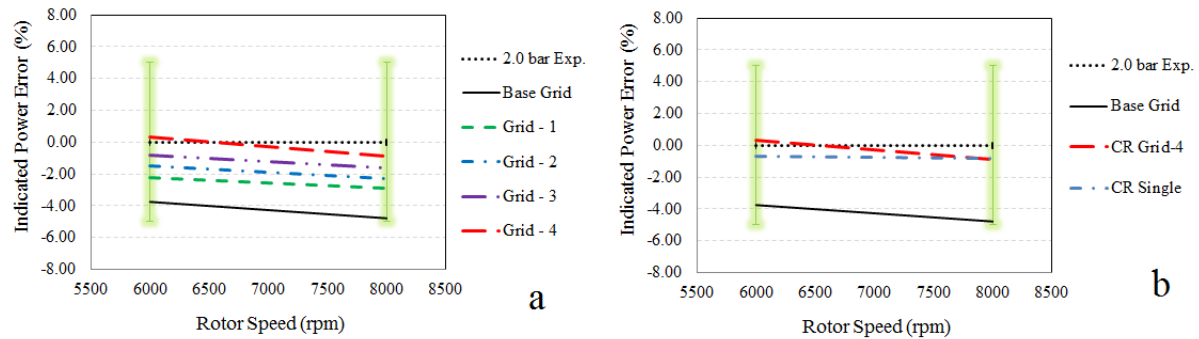


Figure 16 Comparison of indicated power – a) Interlobe refinement of CR grids, b) Single domain grid

Figure 16a shows the comparison of indicated power obtained on RC and successively refined CR grids with non-conformal interface between two rotor domains. The difference in  $P_i$  between CFD prediction and experiment is about  $-3.7\%$  at 6000 rpm and  $-4.8\%$  at 8000 rpm with the RC baseline grid. With the use of CR Grid-1,  $P_i$  predictions have improved for both speeds and at 6000 rpm the difference between predictions and measurements is about  $2.2\%$ . With the grid refinement from CR Grid-1 to CR Grid-4, the under-prediction of power with CFD reduced and with the finest grid CR Grid-4 even overpredicted power for about  $+0.4\%$  at 6000 rpm. It should be noted that all these cases show increase in under-predicting power with the increase in speed.

Figure 16b shows the comparison between indicated powers calculated on RC-3, CR Grid-4 and CR Grid-5 with the measured results. Even though the grid refinement in CR Grid-5 with single domain mesh is equivalent to the baseline RC-3 grid, a substantial improvement in prediction of indicated power was achieved. The results are within  $1\%$  with measurements for all calculated compressor speeds showing that the single domain grid for rotor domains will have significant advantage in calculating power accurately. This supports conclusions made in section 5.2 about the influence of the grid with a single domain on the solution. Indicated power measurement uncertainty in Figure 16a and Figure 16b is of the order  $\pm 5\%$  and all grids provide predictions within these range. Inferences from the results regarding single domain CR Grid – 5 being better is based on the deviations within these measurement uncertainty range.

## 5.6 Flow rate - $\dot{m}$

Figure 17 shows variations in predicting flow rates for different grid types and refinements. The predicted flow rates were normalised to the measured flow rates in order to calculate flow rate error values. A negative percentage values indicate under-prediction of the flow rate.

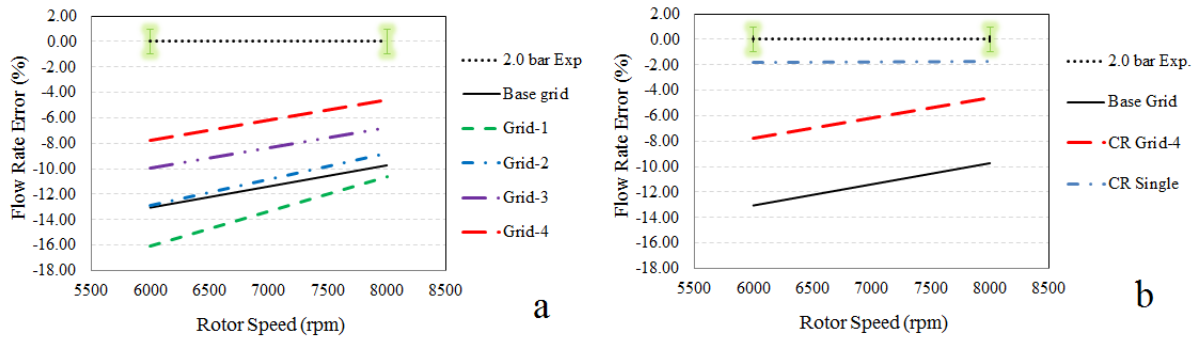


Figure 17 Comparison of normalized flow rates – a) Interlobe refinement of CR grids, b) Single domain grid

Figure 17a shows the comparison of normalised flow rates obtained with the RC-3 baseline grid and the CR type grids with successive refinements from Grid-1 to Grid-4. An interlobe grid refinement greatly influences the flow rate. With the baseline grid RC-3, the difference between CFD prediction and experiment was about  $-13\%$  at 6000 rpm and  $-10.0\%$  at 8000 rpm. The error obtained with refined Grid – 4 reduced to  $-8.0\%$  at 6000 rpm and  $-4.5\%$  at 8000 rpm. The increase in the flow rate with the refinement of grid corresponds to the increase in the indicated power shown in Figure 16. However, the trend of the flow rate vs. speed and power vs. speed curves is opposite since the error in flow rate reduces with speed while the error in predicting power increases with speed.

Since all grids in this diagram are with two domains and non-conformal interface, this over prediction of leakage flow may be associated with numerical error in calculating fluxes over the interface in CFD solver, as mentioned in section 5.2. In addition it is possible that the clearance gap of 60 micro meters which has been used when the grids are calculated does vary due to thermal deformations and other operating uncertainties.

Figure 17b shows the comparison of normalised flows calculated on RC-3, CR Grid-4 and CR Grid-5 with measured results. Similarly, to what is observed with prediction of  $P_i$ , a substantial improvement in prediction of flow is noticed with the CR Grid-5 which has single domain for both rotors and relatively moderate grid size equivalent to that one of the baseline RC-3 grid. The calculation on a single domain grid gave under prediction of flow for just about  $-1.8\%$  and the error was constant at both the speeds. Flow measurement uncertainty in Figure 17a and Figure 17b is of the order  $\pm 1\%$ . Inferences from the results regarding single domain CR Grid – 5 being better is based on the deviations within these measurement uncertainty range.

### 5.7 Volumetric efficiency - $\eta_v$

Volumetric efficiency is the ratio of the actual volume flow rate and the theoretical capacity of the machine normalised to suction conditions. Higher values indicate better sealing of the machine and more efficient compression process.

$$\eta_v = \frac{\dot{V}}{\dot{V}_t} \quad (2)$$

The volume flow rate is calculated from the mass flow rate and suction density using the following equation;

$$\dot{V} = \frac{60 \dot{m}}{\rho_0} \quad (3)$$

The theoretical capacity  $\dot{V}_t$  of the machine is the geometric function of the rotor profile and is defined as the swept volume per revolution multiplied by the compressor speed. It is possible to extract the swept volume directly from a CAD model of the machine or it can be obtained analytically. Figure 18 shows variations of volumetric efficiency calculated using equation 2 for variety of grid type and refinements, as explained in the previous two sections.

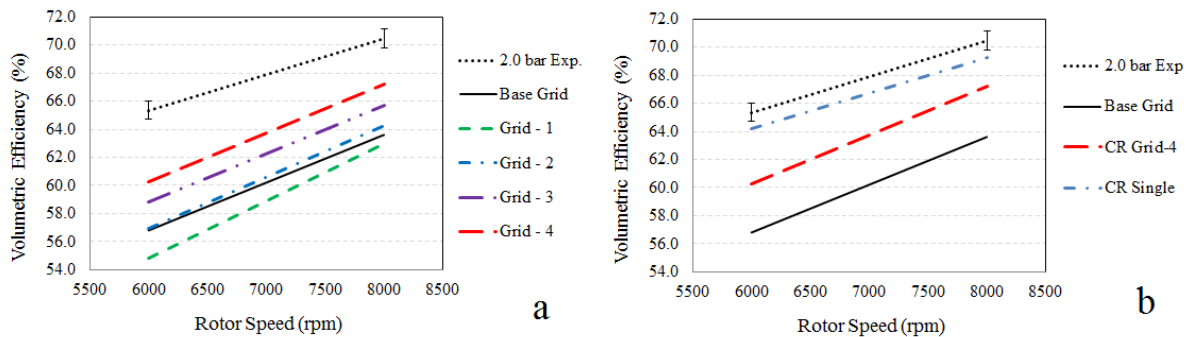


Figure 18 Comparison of volumetric efficiency – a) Interlobe refinement of CR grids, b) Single domain grid

Figure 18a shows volumetric efficiency obtained on RC and successively refined CR grids with non-conformal interface between two rotor domains. Similar to the flow rate, the refinement of the interlobe grid influences the volumetric efficiency. The RC-3 baseline grid gives about 8% lower  $\eta_v$  than the experiment at both speeds. With use of the new CR type grid the difference reduces as the interlobe region is refined so that with CR Grid-4 the difference from the experiment is just about 4%. In line with the flow prediction, the difference is smaller at 8000rm than at 6000rpm.

Figure 18b shows the comparison of volumetric efficiencies calculated on RC-3, CR Grid-1 and CR Grid-5 and measured results. The grid size of CR Grid-5 is equivalent to RC-3 baseline grid but the improvement in prediction of  $\eta_v$  is significant. With the single domain grid the calculation error is just around 1% at both speeds which is a big improvement in comparison to the RC type base grids.

### 5.8 Specific Indicated Power - $P_{si}$

Specific power is a single parameter which gives an indication of the overall thermodynamic performance of a compressor. It is calculated as the power consumed by the compressor to deliver a unit quantity of the compressed gas at certain pressure.  $P_{si}$  is influenced by prediction of both the indicated power and the mass flow rate and is calculated using equation 4. A lower specific power indicates better performance of a compressor.

$$P_{si} = \frac{P_i}{\dot{V} 1000} \quad (4)$$

Figure 19a gives the comparison of specific indicated power obtained on RC and successively refined CR grids with non-conformal interface between two rotor domains. The interlobe grid refinement of the CR grid type is influencing the specific power value as it changes the flow and power prediction. The RC-3 baseline grid predicts higher specific indicated power than the experiment at both speeds. The same trend is observed with new CR grids with non-conformal interface as shown in Figure 16a. However, the refinement of the interlobe domain from Grid-1 to Grid-4, reduces difference between the calculated and measured specific indicated power. With the RC type grid, at 6000rpm the difference between calculated and measured  $P_{si}$  is about 0.25 kW/m<sup>3</sup>/min and it is reduced to about 0.13 kW/m<sup>3</sup>/min at 8000rpm. With CR type Grid – 4, at 6000rpm the difference in  $P_{si}$  is about 0.17 kW/m<sup>3</sup>/min at 6000 rpm and about 0.1 kW/m<sup>3</sup>/min at 8000rpm

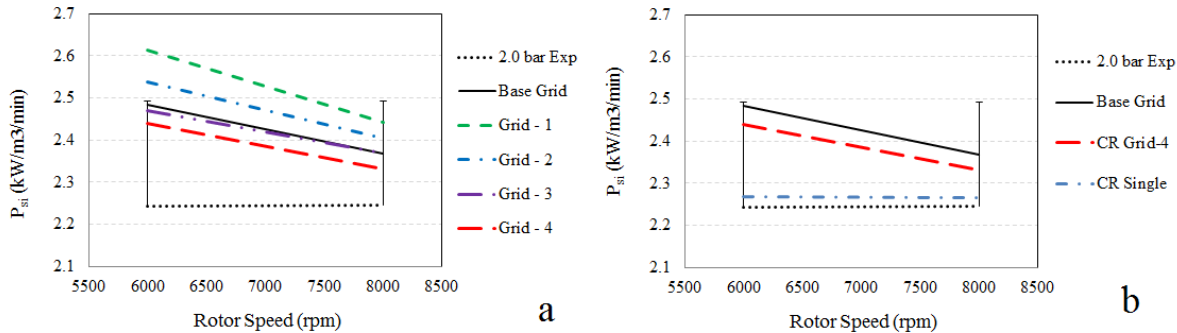


Figure 19 Comparison of specific indicated power – a) Interlobe refined grid, b) Single domain grid

Figure 19b shows the comparison of specific indicated power calculated on RC-3, CR Grid-1 and CR Grid-5 with measured results. Similarly to the prediction of  $P_i$  in Figure 16b and prediction of the flow rates in Figure 17b, the single domain grid CR Grid-5 shows significant improvement in prediction of  $P_{si}$ . With the single domain grid structure the difference is an order of magnitude lower at just about 0.02 kW/m<sup>3</sup>/min and is consistent at both speeds.

A noticeable difference is observed in the trend of  $P_{si}$  with speed. In case on RC and the CR two domain grids with non-conformal interface,  $P_{si}$  decreased at 8000rpm compared to 6000rpm. But with CR single domain grid  $P_{si}$  it follows the same trend as the measured values. This difference is an influence of the relative prediction of  $\dot{m}$  and  $P_i$ , assumption of a constant  $\eta_m$ , fixed clearance size and also is due to the elimination of non-conformal interface between the rotors.

## 5.9 Case study observations

- The non-conformal interface between the rotors was better resolved because of interlobe grid refinement in CR type grids Grid-1 to Grid-4.

- The compression part of pressure curve showed that there was a very small difference between the base grid and the new grids and the increase in the internal pressure is aligned well with the experimental results.
- From Grid-1 to Grid-4, the peak internal pressure showed a small increase.
- CR Grid-5 with single domain showed a higher peak pressure. It is believed that this is because this mesh avoids the use of a non-conformal interface which in CFD solvers may produce non-physical losses due to the lack of conservativeness.
- Indicated power increased by a small amount from Grid-1 to Grid-4 but was close to the experimental value at both speeds. Single domain CR Grid-5 showed the highest accuracy in prediction of indicated power.
- There was a big influence of the interlobe grid refinement on the predicted leakage flows and hence the mass flow rate. The single domain mesh CR Grid-5 showed the highest accuracy in the flow prediction with the error of just 1.8% at both speeds.
- A difference between CFD calculations and experimentally obtained results still exists. This can be attributed to the choice of operational non-variable clearance gaps in the CFD model.
- In order to obtain higher accuracy in CFD predictions, change in the size of leakage gaps due to thermal deformation needs to be accounted for in the CFD models. This requires employment of fluid solid interaction modelling or using measured clearance data. The new grid generation approach however provides the flexibility to improve the resolution of the rotor geometry and thereby to some extent reduces the inaccuracy in leakage flow calculations.
- Similarly, generation of a single mesh block for the rotors has greatly contributed towards the improved accuracy of the numerical solution.

## 6 Conclusion

In the Part I of this paper an algebraic generation of single domain computational grid for screw machines has been formulated. The method combines the robustness, speed and numerical accuracy of a single domain CR type mesh with the speed and control of algebraic grid generation. A new algorithm for boundary distribution of CR type grid with background blocking was implemented. It allowed the control of the interlobe region and eliminate the non-conformal interface between the two rotor blocks, while still maintaining fully hexahedral cell structure. In this Part II of the paper a test case has been presented to report the influence of various grid generation approaches on the accuracy of the performance prediction. A grid independency study was conducted on the baseline grid of the RC type and a sufficient size of the computational grid was identified for a balance of accuracy of solution and computational resource for CFD calculation. Based on this, the new CR grid structure was used to generate a set of rotor grids with successive refinements in the interlobe region. Additionally, a CR grid type with a single domain for two rotors was generated by use of background blocking to produce

conformal map and then remove it by merging cells on the interface in order to produce the single domain mesh.

The performance predictions with all these grids were compared through the chamber internal pressure history, and the set of integral performance parameters such as mass flow rate, indicated power, volumetric efficiency and specific indicated power.

The CR Gird-5 with the single domain rotors grid, produced the lowest leakage through the leakage paths with the highest accuracy compared to measurements. This is attributed to the method which CFD solvers use to calculate fluxes over non-conformal interfaces and shows that these are not fully conservative as it would be expected. It is recommended that the use of such non-conformal interfaces is avoided if possible.

A factor of uncertainty remains in terms of variation in the clearance size due to thermal deformations during the operation of the machine. It is in particular important for oil free compressors. Considering this, for a set clearance size in the rotor computational meshes, the best performance prediction was achieved by use of the new CR grid with a single domain for both rotors. In comparison to the base grid of RC type, successive refinement in the interlobe region improved mass flow prediction but the sensitivity was much lower than in the case of single domain mesh where the non-matching interface between the rotors was eliminated. The influence of the refinement of the interlobe domain in a single domain mesh still remains to be evaluated.

The developments described in the Part I and Part II of this paper have allowed extension of the capability of the deforming grids generated using algebraic methods to be used with other CFD solvers like STAR CCM+ and ANSYS FLUENT. A full hexahedral cell structure and improved global grid quality makes it possible for addition of more complex physical phenomenon with the gas compression calculations like oil injection and multiphase flows.

## References

1. Kethidi M., Kovačević A., Stošić N., Rane S., 2012. Modelling of turbulence in screw compressor flows, Proc. Turbulence, Heat and Mass Transfer 7, E308.
2. Kovačević A., 2002. Three-Dimensional Numerical Analysis for Flow Prediction in Positive Displacement Screw Machines, Ph.D. Thesis, School of Engineering and Mathematical Sciences, City University London.
3. Kovačević A., Stošić N., Smith I. K., 2006. Numerical simulation of combined screw compressor-expander machines for use in high pressure refrigeration systems, Simulation Modeling Practice and Theory, Volume 14, Issue 8, Pages 1143–1150.
4. Kovačević A., Stošić N. and Smith I. K., 2007. Screw compressors - Three dimensional computational fluid dynamics and solid fluid interaction, ISBN 3-540-36302-5, Springer-Verlag Berlin Heidelberg New York.

5. Kovačević A. and Rane S., 2013. 3D CFD analysis of a twin screw expander, 8th International conference on compressors and their systems, London, p. 417.
6. Kovačević A., Rane S., Stošić N., Jiang Y., Furmanczyk M. and Lowry S., 2014. Influence of approaches in CFD Solvers on Performance Prediction in Screw Compressors, Proc. Int. Compressor Conf. at Purdue, Paper 1124.
7. Papes, I., Degroote, J., Vierendeels, J., 2014. 3D CFD analysis of a twin screw expander for small scale ORC systems. Proceedings of the 11th World Congress on Computational Mechanics. pp. 7207–7217.
8. Pascu M., Kovacevic A., and Udo N., 2012, Performance optimization of Screw Compressors based on numerical investigation of the flow behaviour in the discharge chamber. Int Compressor Conf at Purdue, Purdue, p. 1145.
9. Rane S., Kovačević A., Stošić N. and Kethidi M., 2013. Grid Deformation Strategies for CFD Analysis of Screw Compressors, Int Journal of Refrigeration, 36, 7, p. 1883-1893.
10. Rane S., Kovačević A., Stošić N. and Kethidi M., 2014. Deforming grid generation and CFD analysis of variable geometry screw compressors, Computers and Fluids, 99, p. 124–141.
11. Sauls J. and Branch S., 2013. Use of CFD to develop improved one-dimensional thermodynamic analysis of refrigerant screw compressors. 8th Int conf on compressors and their systems, p. 591.
12. Stošić N., Smith I.K. and Kovačević A., 2005. Screw Compressors: Mathematical Modeling and Performance Calculation, Monograph, Springer Verlag, Berlin, June 2005, ISBN: 3-540-24275-9.
13. Vande Voorde J., Vierendeels J., Dick E., 2004. A Grid Generator for flow calculations in Rotary Volumetric Compressors, European Congress on Computational Methods in Applied Sciences and Engineering.
14. Vande Voorde J., 2005. Numerical flow calculations in rotary positive-displacement machines. PhD Thesis. Ghent University.
15. Bianchi G., Cipollone R., 2015, Friction power modelling and measurements in sliding vane rotary compressors. *Applied Thermal Engineering* 84, 276-285.
16. Rane S., 2015. Grid generation and CFD analysis of variable geometry screw machines. PhD Thesis. City, University of London.
17. Bianchi G., Cipollone R., 2015, Theoretical modelling and experimental investigations for the improvement of the mechanical efficiency in sliding vane rotary compressors. *Applied Energy* 142, 95-107.
18. Rane S., Kovačević A., 2017, Algebraic Generation of Single Domain Computational Grid for Twin Screw Machines. Part I. Implementation. *Advances in Engineering Software*. d.o.i: 10.1016/j.advengsoft.2017.02.003